AIAA JOURNAL
Vol. 35, No. 1, January 1997

Cartesian Boundary Treatment of Curved Walls for High-Order Computational Aeroacoustics Schemes

Konstantin A. Kurbatskii* and Christopher K. W. Tam†
Florida State University, Tallahassee, Florida 32306-3027

It is known that the use of high-order central difference schemes on a Cartesian grid is preferable for the computation of acoustic wave propagation problems. Those schemes tend to be less dispersive and dissipative than most other types of schemes. They are also more capable of providing an accurate wave speed. A Cartesian boundary treatment for problems involving the scattering of acoustic waves by solid objects with curved boundary surfaces, designed to be used in conjunction with such high-order central difference schemes, is proposed. The development of this method is based on the observation that a solid wall actually exerts a pressure force on the fluid to keep it from flowing across the wall surface. In this method, ghost values of pressure are introduced at mesh points adjacent to the solid boundary inside the object. The ghost values are then chosen so that the solid wall boundary condition is satisfied. The method is also applicable to objects with sharp corners. Numerical examples are provided.

I. Introduction

MANY aeroacoustics problems, especially those in the areas of duct acoustics and turbomachinery noise, involve the interaction of acoustic waves and curved solid surfaces. Accurate numerical solutions of these problems require high-quality computation schemes as well as good boundary treatments. This paper reports the development of a curved wall boundary treatment for use in conjunction with high-order finite difference schemes on Cartesian grids.

In computational fluid dynamics (CFD) there are two general approaches for treating curved wall boundaries. They are the composite body-fitted grids[1] and the unstructured-grids[2] methods. In using composite body-fitted grids, the physical plane is mapped into a computational plane. The mapping or transformation introduces variable coefficients into the equations of motion. Thus for wave propagation problems, the numerical waves effectively propagate through an inhomogeneous medium in the computation domain. Unstructured grids, on the other hand, create irregular numerical interfaces all over the physical space. In contrast, methods that use regular Cartesian grids are free from these types of artificial inhomogeneities. For time-independent CFD problems, these artificial inhomogeneities have no adverse effects on the numerical solutions. For aeroacoustics problems, which are time dependent, they could cause undesirable refraction and scattering of the sound waves. In some cases, these numerical inhomogeneities could even lead to nonuniform wave speed.

Many CFD codes, especially those designed for unstructured grids, use finite volume formulation or other low-order schemes. For time-independent problems, these low-order schemes have been found to perform well. In a recent article, Tam[3] discussed some of the major differences between CFD and computational aeroacoustics (CAA) problems. In CAA, the major concerns are numerical dispersion, dissipation, and inaccurate wave speed errors. These requirements are satisfied by high-order finite difference schemes on Cartesian grids. Low-order schemes generally do not perform as satisfactorily. Therefore, high-order schemes on Cartesian grids are preferred for solving CAA problems. An example of such a CAA scheme is the dispersion-relation-preserving (DRP) scheme.[4]

Received June 11, 1996; revision received Sept. 30, 1996; accepted for publication Oct. 11, 1996; also published in *AIAA Journal on Disc*, Volume 2, Number 2.

*Graduate Student, Department of Mathematics.
†Professor, Department of Mathematics. Associate Fellow AIAA.

In a recent work on the reflection of sound waves off plane solid surfaces, Tam and Dong[5] introduced the idea of using ghost values of pressure to form boundary treatments for high-order finite difference schemes. Their motivation was the need for an extra set of conditions at wall boundaries to enforce the wall boundary conditions. They chose ghost values of pressure to simulate the wall pressure computationally.

When the order of the finite difference equations of a computation scheme is higher than that of the original partial differential equations, extra boundary conditions, other than those of the physical problem, are required to define a unique solution. In the boundary treatment of Tam and Dong,[5] the need for such additional boundary conditions was avoided by using backward difference stencils in the wall region. For the case of plane acoustic waves incident on a plane wall, which is aligned with the grid lines, the entire finite difference problem, including boundary treatment, can be solved analytically. Tam and Dong performed such an analysis and reported that their ghost point boundary treatment led to good agreements with the exact solutions.

The purpose of this investigation is to extend the ghost point boundary treatment of Tam and Dong[5] to general curved solid surfaces. We will confine our consideration to two-dimensional acoustic wave scattering problems. The extension from flat to curved solid surfaces turns out to be totally nontrivial. Several major difficulties have to be overcome. It is easy to show in the case of curved surfaces that there is a coupling of the ghost values. The domain of influence of a ghost value is no longer along a single grid line alone.

In CFD, Cartesian boundary schemes are not currently as popular as composite body-fitted grids and unstructured-grid methods. The reasons are complicated. They will not be discussed here as they are not relevant to aeroacoustics computation. For the same reason, a detailed survey of the literature will not be done. Suffice to say, Refs. 6–19 offer a set of representative samples of the various Cartesian grid approaches and emphasis considered by different investigators. The majority of the schemes have been developed for steady-state, transonic flow calculations using finite volume methodology. The works of Berger and LeVeque,[8] Chiang et al.,[11] and Quirk[18] deal with unsteady flows. But their emphasis is on the interaction between shock waves and solid surfaces. As far as we are able to find, there is an almost total absence of any investigations on acoustic wave scattering problems by curved surfaces with the exception of Chung and Morris.[20] In their treatment, Chung and Morris replaced the solid bodies by fluids of very low density. Thus, the wall surfaces became surfaces of impedance mismatch, which exhibited characteristics closely approximating those of a solid surface. Our approach is, however, fundamentally different. The advantages and disadvantages of the two methods are also very different.

The rest of this paper is as follows. A general classification of ghost points is provided in Sec. II. This classification offers a complete catalog of possible geometric configurations of the relative positions of the boundary curve and ghost points. In Sec. III, the rules by which the wall boundary condition is enforced are established. To suppress the generation of spurious numerical waves at the wall and to provide numerical stability, artificial selective damping is required in the wall boundary region. This is discussed in Sec. IV. Numerical results of the present boundary treatment are given in Sec. V. Examples of the scattering of acoustic waves by smooth objects as well as bodies with sharp edges are included. The computed results are compared with exact solutions, when they are available. Otherwise, they are compared with numerical results computed by a refined mesh. Favorable agreements are found.

II. Classification of Mesh and Ghost Points

Consider small amplitude two-dimensional acoustic disturbances impinging on a solid surface. The governing equations are the linearized Euler equations, which may be written in dimensionless form [with respect to length scale L, velocity scale c (sound speed), time scale L/c, density scale ρ_0 (ambient density), and pressure scale $\rho_0 c^2$] as

$$\frac{\partial \boldsymbol{U}}{\partial t} + \frac{\partial \boldsymbol{E}}{\partial x} + \frac{\partial \boldsymbol{F}}{\partial y} = \boldsymbol{Q} \tag{1}$$

where

$$\boldsymbol{U} = \begin{bmatrix} \rho \\ u \\ v \\ p \end{bmatrix}, \qquad \boldsymbol{E} = \begin{bmatrix} u \\ p \\ 0 \\ u \end{bmatrix}, \qquad \boldsymbol{F} = \begin{bmatrix} v \\ 0 \\ p \\ v \end{bmatrix}$$

The term $\boldsymbol{Q}$ on the right-hand side of Eq. (1) represents acoustic sources. On the solid surface, the physical boundary condition is

$$\boldsymbol{V} \cdot \boldsymbol{n} = 0 \tag{2}$$

where $\boldsymbol{n}$ is the unit outward pointing normal of the surface and $\boldsymbol{V}$ is the velocity vector. By taking the dot product of the momentum equations of Eq. (1) with $\boldsymbol{n}$, it is easy to show, in the absence of surface acoustic sources, that boundary condition (2) is equivalent to

$$\frac{\partial p}{\partial n} = 0 \tag{3}$$

It will be assumed that Eq. (1) is to be solved by a high-order finite difference scheme. Without loss of generality, the 7-point stencil DRP scheme[4] will be used throughout as a model of high-order finite difference schemes. The discretized form of Eq. (1) on a Cartesian grid according to the DRP scheme is

$$\boldsymbol{U}_{\ell,m}^{(n+1)} = \boldsymbol{U}_{\ell,m}^{(n)} + \Delta t \sum_{j=1}^{3} b_j \boldsymbol{K}_{\ell,m}^{(n-j)} \tag{4}$$

$$\boldsymbol{K}_{\ell,m}^{(n)} = -\frac{1}{\Delta x} \sum_{j=1}^{3} a_j \boldsymbol{E}_{\ell+j,m}^{(n)} - \frac{1}{\Delta y} \sum_{j=1}^{3} a_j \boldsymbol{F}_{\ell,m+j}^{(n)} + \boldsymbol{Q}_{\ell,m}^{(n)} \tag{5}$$

where ℓ and m are the indices of the mesh points in the x and y directions, respectively; Δx and Δy are the mesh sizes in the x and y directions; Δt is the time step; and superscript n is the time level. The stencil coefficients b_j and a_j are given in Ref. 3.

The central issue to be discussed here is how to develop and implement an appropriate discretized boundary condition that is equivalent to Eq. (2) or Eq. (3) for an arbitrary curved surface. In this work, the wall boundary condition will be enforced by the use of ghost values of pressure prescribed at the ghost points following the idea of Tam and Dong.[5] However, before considering curved wall surfaces with numerous possible kinds of complexities, it is deemed prudent to first review briefly the basic concepts of ghost values and ghost points.

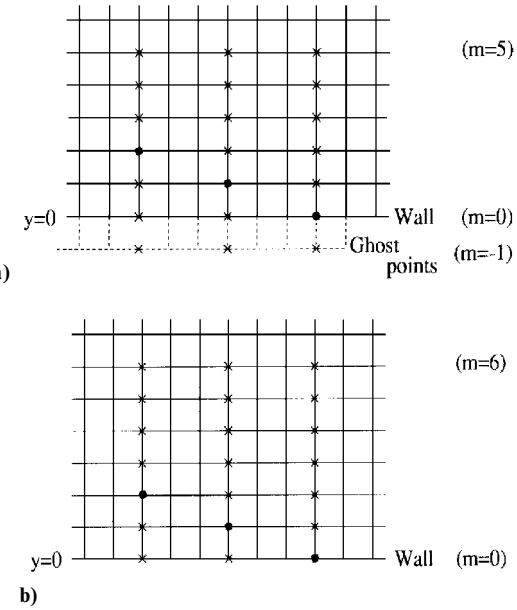

Fig. 1 Seven-point stencils used to compute a) y-derivatives of p and b) y-derivatives of ρ, u, and v in the boundary region near a wall at $y = 0$.

A. Concept of Ghost Points and Ghost Values

Consider the reflection of sound waves by a plane wall located at $y = 0$ as shown in Fig. 1. For the three rows of points adjacent to the wall, a 7-point finite difference stencil used to approximate the y derivative will involve points outside the computation domain and, therefore, cannot be implemented. To keep the stencil inside the computation domain, backward differences may be used. It is desirable to require the discretized form of governing equation (1) to be satisfied at points on the wall. This is the case for the solution of the original partial differential equations. However, this will make it impossible to satisfy the boundary condition, as there will be more equations than dependent variables. To allow the finite difference solution to satisfy the wall boundary condition, Tam and Dong[5] suggested the introduction of a row of ghost points below the wall (see Fig. 1a) where a set of ghost values of pressure is prescribed. These ghost values of pressure simulate the actual pressure exerted by the wall on the fluid. The proposal is to compute all of the y derivatives according to the backward difference stencils shown in Fig. 1. The quantities $\partial\rho/\partial y$, $\partial u/\partial y$, and $\partial v/\partial y$ are all calculated using values of the variables lying inside the physical domain. For the y derivative of p, the stencil extends to the ghost point below the wall. The ghost value of p, i.e., $p_{\ell,-1}^{(n)}$, is to be chosen so that $v_{\ell,0}^{(n)}$ is zero for all n. This is accomplished through the discretized form of the y-momentum equation, namely, the third equation of Eqs. (4) and (5). On writing out in full, the discretized y-momentum equation at $m = 0$ becomes

$$v_{\ell,0}^{(n+1)} = v_{\ell,0}^{(n)} + \Delta t \sum_{j=1}^{3} b_j K_{\ell,0}^{(n-j)} \tag{6}$$

$$K_{\ell,0}^{(n-j)} = -\frac{1}{\rho_0 \Delta y} \sum_{i=1}^{5} a_i^{15} p_{\ell,i}^{(n-j)} \tag{7}$$

where a_i^{15} are the optimized coefficients of the backward differences stencil of the DRP scheme.[3] Equations (6) and (7) are to be used to find $v_{\ell,0}^{(n+1)}$ after all of the physical quantities are found at the end of the nth time level. To ensure the wall boundary condition $v_{\ell,0}^{(n+1)} = 0$ is satisfied, the ghost value $p_{\ell,-1}^{(n)}$ may be found by setting $v_{\ell,0}^{(n+1)} = 0$ in these equations. Upon solving for $p_{\ell,-1}^{(n)}$, it is easy to find

$$p_{\ell,-1}^{(n)} = -\frac{1}{a_{-1}^{15}} \sum_{i=0}^{5} a_i^{15} p_{\ell,i}^{(n)} \tag{8}$$

It is easy to see that Eq. (8) is tantamount to setting the ghost value so that $\partial p/\partial y = 0$ at the wall. This is the same as boundary condition (3).

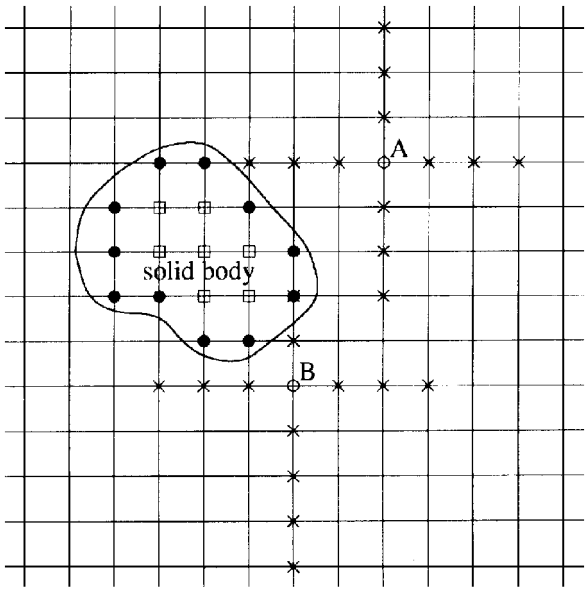

Fig. 2 Schematic diagram showing a solid body in a Cartesian mesh; also shown are ● ghost points and □, exterior points.

B. Interior, Exterior, Boundary, and Ghost Points

We will now consider solving acoustic wave scattering problems involving a solid body with curved surfaces computationally on a Cartesian grid. For clarity and convenience of reference, each Cartesian mesh point inside the computation domain will be referred to as an interior, exterior, boundary, and ghost point depending on its location relative to the boundary curve of the body. This classification has proven to be very useful to the programming effort. Let the body be represented analytically by $S(x, y) \leqslant 0$. The boundary curve is given by the equality sign, i.e., $S(x, y) = 0$. We will adopt the following definitions:

1) Interior point: (ℓ, m) is an interior point (inside fluid region) if $S(\ell\Delta x, m\Delta y) \geqslant 0$.

2) Exterior point: (ℓ, m) is an exterior point (inside body) if $S(\ell\Delta x, m\Delta y) < 0$.

3) Boundary point: (ℓ, m) is a boundary point if it is an interior point and one or more of the points $(\ell + i, m), (\ell, m + j), i, j = \pm 1, \pm 2, \pm 3$ (points in the 7-point stencil), is an exterior point.

4) Ghost point: (ℓ, m) is a ghost point if it is an exterior point and one or more of its nearest neighbors, i.e., $(\ell + i, m), (\ell, m + j), i = \pm 1, j = \pm 1$, is an interior point.

Figure 2 gives a simple illustration of the various types of points. For instance, in Fig. 2 B is a boundary point and A is an interior point.

C. Classification of Ghost Points

In the proposed boundary treatment the solid body is simulated by the ghost values of pressure at the ghost points. For this to be an accurate representation of the body, the mesh size of the Cartesian grid must have been chosen so that it can provide an adequate resolution of the surface geometry (boundary curve). For instance, the boundary curve must not cut the mesh line between two grid points more than once. It will be assumed that this is true throughout this work. Since sound waves propagate without a preferred direction, a square mesh with $\Delta x = \Delta y$ will, in general, be used. This will be assumed to be the case.

It is self-evident that to be able to implement the present ghost point method automatically in a computer, a systematic classification of the relative geometry of the ghost points and the boundary curve of the body is necessary. Here it can be shown, to within a simple rotation or reflection, that all ghost points may be classified into five types with minor variations, i.e., subclassifications within a particular type. The type classification depends only on whether the four nearest neighbors of a ghost point are interior or exterior points. The subclassification depends on whether those nearest neighbors that are exterior points are also ghost points.

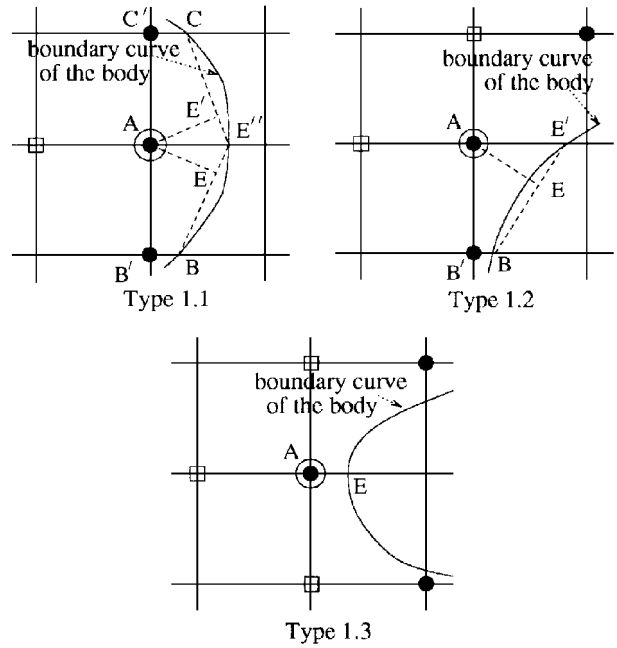

Fig. 3 Configurations of type 1 ghost points; *A* is the ghost point under consideration.

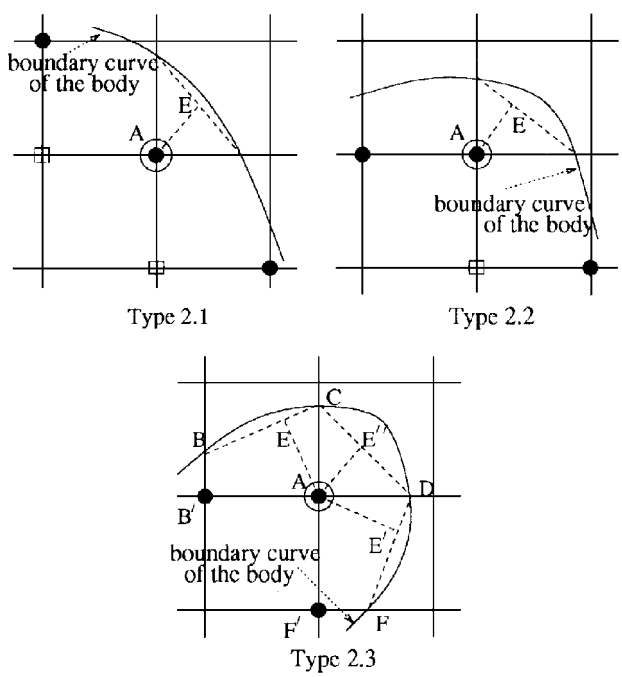

Fig. 4 Configurations of type 2 ghost points.

Type 1 Ghost Point

A ghost point is a type 1 ghost point if three of its nearest neighbors are exterior points. According to whether the nearest neighbors, which are exterior points, are also ghost points or not, there are three possible variations as shown in Fig. 3. They will be referred to as type 1.1, 1.2, and 1.3 ghost points.

Type 2 Ghost Point

A ghost point is a type 2 ghost point if two of its nearest neighbors are exterior points and these two neighbors are themselves diagonally immediate neighbors (see Fig. 4). Within type 2 ghost points, there are three possible geometrical arrangements. For identification purposes, these ghost points are labeled as type 2.1, 2.2, and 2.3 ghost points.

Type 3 Ghost Point

A ghost point is a type 3 ghost point if two of its nearest neighbors are exterior points but they are not diagonally immediate neighbors.

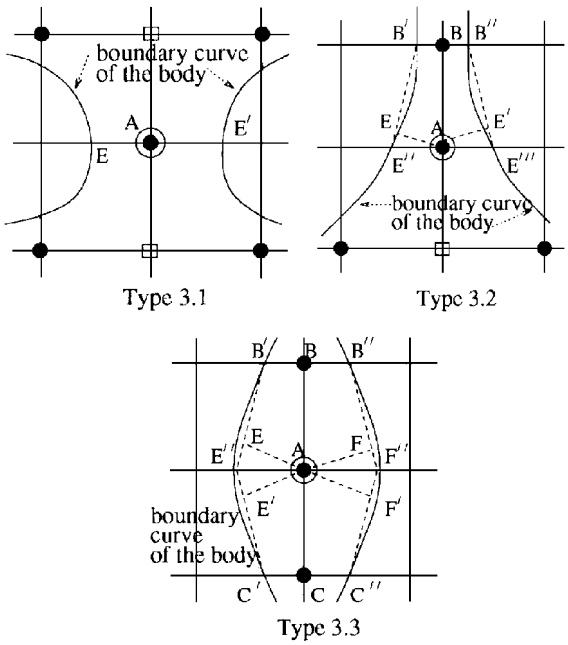

Fig. 5 Configurations of type 3 ghost points.

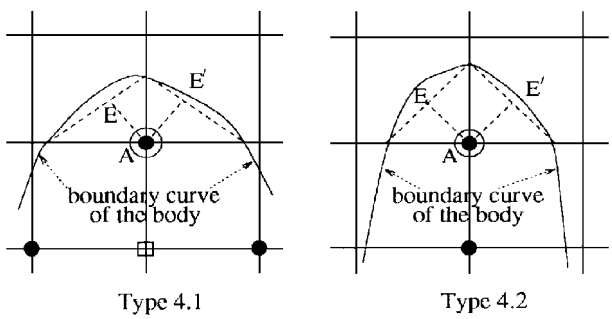

Fig. 6 Configurations of type 4 ghost points.

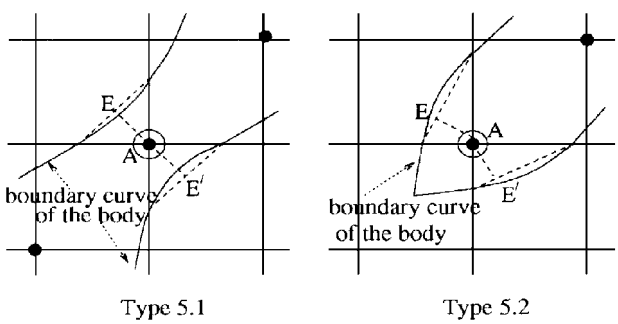

Fig. 7 Configurations of type 5 ghost points.

Again, there are three possible variations within this type, as shown in Fig. 5. They are designated as type 3.1, 3.2, and 3.3 ghost points.

Type 4 Ghost Point

A ghost point is a type 4 ghost point if only one of its nearest neighbors is an exterior point. This neighbor may be a ghost point or just an exterior point. Thus, there are two subtypes, type 4.1 and 4.2 ghost points, as shown in Fig. 6.

Type 5 Ghost Point

A ghost point is a type 5 ghost point if none of its nearest neighbors are exterior points. In this case there are two subtypes, namely, type 5.1 and 5.2 ghost points, as shown in Fig. 7.

III. Enforcement of Wall Boundary Condition

In introducing the concept of ghost points and ghost values, it is apparent that, for the case of a plane wall, one ghost value of pressure per ghost point would suffice. However, for thin bodies simulated by the type 5 ghost points (see Fig. 7) the ghost points are responsible for two boundaries. To be able to enforce the wall boundary condition on both boundaries, two ghost values of pressure must be assigned to each ghost point. Thus, depending on the type or subtype of ghost point, there may be one or two ghost values of pressure associated with it.

A. Enforcement Points for Curved Walls

With a finite number of ghost points, the wall boundary conditions can only be enforced at a limited number of points on the boundary curve of the solid body. In this work, information about the body geometry between the mesh lines of the Cartesian grid will not be retained. The body will be approximated by straight line segments between successive intersection points between the boundary curve of the body and the grid lines. In Figs. 3–7 the approximated body shape is shown in broken lines. Now, for each ghost value, the wall boundary condition (2) or (3) will be enforced at the point on the straight line boundary segment that is closest to the ghost point. The enforcement point for each type of ghost point can be standardized once and for all. Table 1 is a summary of the appropriate enforcement points for each type of ghost point. This table also gives the number of ghost values for the various types of ghost points.

B. Determination of the Ghost Values of Pressure

As in the case of a plane wall, the ghost values of pressure are determined only after the values of ρ, u, v, and p are computed at all interior points at a given time level. Their numerical values are assigned so that the wall boundary condition is satisfied at all of the enforcement points at the next time level. Since most enforcement points are not mesh points, information concerning the pressure gradient at these points can only be obtained by interpolation or extrapolation. In this work, a two-step extrapolation/interpolation process is carried out. To illustrate this, consider the configuration shown in Fig. 8. To find the values of $\partial p/\partial x$ and $\partial p/\partial y$ at the enforcement point E at the end of time level n, these derivatives are first found at the grid-line boundary-curve intersection points A and

Table 1 Enforcement points of wall boundary condition

Type of ghost point	Number of ghost values	Enforcement point	Condition	Reference figure
1.1	1	E	if $B/B < AE/\!/, C/C$	3
		$E/$	if $C/C < AE/\!/, B/B$	3
		$E/\!/$	if $AE/\!/ \leq B/B, C/C$	3
		$E/\!/$	if $AE/\!/ \geq B/B, C/C$	3
1.2	1	E	if $B/B < AE/$	3
		$E/$	if $AE/ \leq B/B$	3
1.3	1	E		3
2.1	1	E		4
2.2	1	E		4
2.3	2	E	if $B/B \leq AC$	4
		$E/\!/$	if $AC \leq B/B$	4
		$E/$	if $F/F \leq AD$	4
		$E/\!/$	if $AD \leq F/F$	4
3.1	2	E and $E/$		5
3.2	2	E	if $BB/ \leq AE/\!/$	5
		$E/\!/$	if $AE/\!/ \leq BB/$	5
		$E/$	if $BB/\!/ \leq AE/\!/$	5
		$E/\!/$	if $AE/\!/ \leq BB/\!/$	5
3.3	2	E	if $BB/ \leq AE/\!/, CC/$	5
		$E/$	if $CC/ \leq AE/\!/, BB/$	5
		$E/\!/$	if $AE/\!/ \leq BB/, CC/$	5
		F	if $BB/\!/ \leq AF/\!/, CC/\!/$	5
		$F/$	if $CC/\!/ < AF/\!/, BB/\!/$	5
		$F/\!/$	if $AF/\!/ \leq BB/\!/, CC/\!/$	5
4.1	2	E and $E/$		6
4.2	2	E and $E/$		6
5.1	2	E and $E/$		7
5.2	2	E and $E/$		7

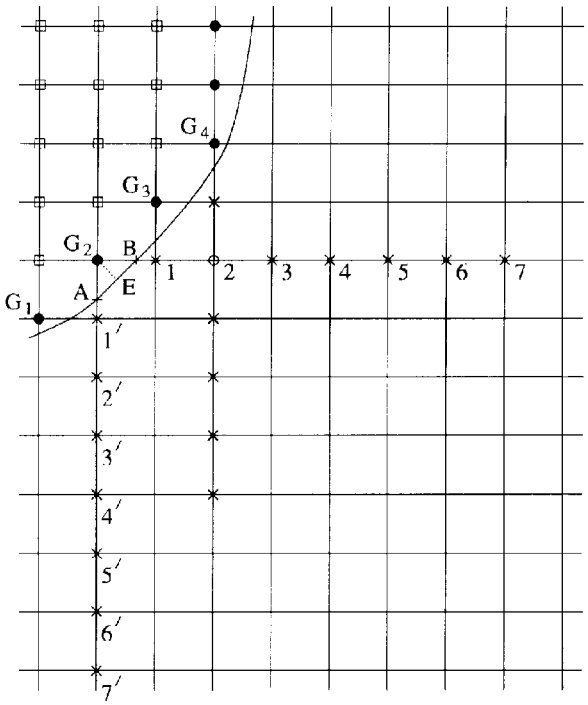

Fig. 8 Points used to determine $\partial p/\partial x$ and $\partial p/\partial y$ at A and B, the intersection points of the boundary curve and the Cartesian mesh, by extrapolation.

B. For point A, both $\partial p/\partial x$ and $\partial p/\partial y$ are calculated by extrapolation from those of the seven interior points $1\prime$–$7\prime$. The derivatives at the interior points are calculated by the 7-point finite difference approximation, either central or backward difference, whichever is appropriate according to the DRP scheme. Some of these differences will, no doubt, contain the still unknown ghost values of pressure at ghost point G_1 and G_2 at time level n. Similarly, the values of $\partial p/\partial x$ and $\partial p/\partial y$ at B at time level n are obtained by extrapolation from the seven interior points 1–7. Again, appropriate central or backward differences are used. Once the derivatives of pressure at A and B are found, they are linearly interpolated to the enforcement point E. Finally, the boundary condition to be satisfied at E is

$$\frac{\partial p}{\partial x}n_x + \frac{\partial p}{\partial y}n_y = 0 \tag{9}$$

where n_x and n_y are the directional cosines of the line G_2E or the normal to the boundary segment AB.

For each ghost value of a ghost point, there is a boundary condition in the form of Eq. (9). Since the ghost values of p at several ghost points are included in Eq. (9), the ghost values of pressure are coupled by a linear system of algebraic equations. These equations can be put into a matrix system. This is one of the major differences between the treatment of a curved solid surface and a flat surface that is parallel to a grid line. In the latter case, there is no coupling of ghost values; i.e., the coefficient matrix of the linear system is diagonal.

The matrix equation may be written in the form

$$\boldsymbol{Ap} = \boldsymbol{b} \tag{10}$$

where $\boldsymbol{p}$ is the column vector of all of the ghost values of pressure. Vector $\boldsymbol{b}$ depends on the value of pressure of the interior points around the body at time level n. It is a known vector. It can be shown that the coefficient matrix $\boldsymbol{A}$ depends only on the geometry of the body and the mesh size of the Cartesian grid. It is independent of the time level. Thus, once $\boldsymbol{A}$ is formed, it is necessary to calculate $\boldsymbol{A}^{-1}$ only once. The ghost values are then found for all subsequent time levels by premultiplying $\boldsymbol{b}^{(n)}$, i.e.,

$$\boldsymbol{p}^{(n)} = \boldsymbol{A}^{-1}\boldsymbol{b}^{(n)} \tag{11}$$

Matrix equation (11) is effectively the discretized form of boundary condition (3). With curved wall boundary condition (11), problems involving acoustic scattering by solid bodies of arbitrary geometry, including those with sharp corners, can be calculated in the time domain by the DRP scheme. It is possible to develop a computer program to form the matrix $\boldsymbol{A}$ and vector $\boldsymbol{b}^{(n)}$ automatically. With such a program, numerical solution of acoustic scattering problems can be done fairly routinely.

IV. Boundary Damping

The approximation involving the replacement of the boundary curve of a body by straight line segments invariably introduces some irregularities in the wall boundary. Such irregularities are quite efficient in generating short spurious numerical waves[21] in the presence of incident acoustic waves. These spurious waves not ony pollute the numerical solution but in many instances could lead to numerical instability. For these reasons, it is important that artificial selective damping be added to the computation stencils especially in the boundary region of the solid surface to damp out these waves or prevent them from being created.

The artificial selective damping stencils given in Ref. 3 are adopted. These stencils are designed so that damping is concentrated primarily on short numerical waves. On incorporating artificial selective damping into the DRP scheme, Eq. (5) becomes

$$K^{(n)}_{\ell,m} = -\frac{1}{\Delta x}\sum_J a_J E^{(n)}_{\ell+J,m} - \frac{1}{\Delta y}\sum_k a_k F^{(n)}_{\ell,m+k} - \frac{L}{\Delta x}\frac{1}{Re_{\Delta x}}\sum_j d_j U^{(n)}_{\ell+j,m} - \frac{L}{\Delta y}\frac{1}{Re_{\Delta y}}\sum_i d_i U^{(n)}_{\ell,m+i} \tag{12}$$

where d_j are the coefficients of the damping stencil and $Re_{\Delta x}$ and $Re_{\Delta y}$ are the mesh Reynolds number ($Re_{\Delta x} = c\Delta x/\nu_a$: ν_a is the artificial kinematic viscosity[3]). The sum over J, k, j, and i in Eq. (12) must be adjusted according to the proximity of the point (ℓ, m) from the wall. The size of the damping stencil may be 3, 5, or 7. The largest stencil is to be used whenever possible.

Because we have assumed $\Delta x = \Delta y$ in this work for convenience, we will use Re_Δ to denote the mesh Reynolds number from now on. In the numerical computations, a spatial distribution of Re_Δ^{-1} in the form of a Gaussian with the largest value at the wall surface and half-width of four mesh spacings in the normal direction is used. Away from the wall Re_Δ^{-1} reaches the background value of 0.025. In each run, the value Re_Δ^{-1} at the wall is incrementally adjusted until a stable solution is obtained. Also 3-point stencil artificial damping is applied only to the momentum equations. Because of the existence of ghost values of pressure, its use on the energy equation (the equation to update p) near the wall including the ghost values would introduce excessive numerical damping.

V. Numerical Results

A computer program has been developed that automatically implements the Cartesian boundary treatment discussed. Once the mesh size is fixed and the boundary curve of the body specified, the program identifies the ghost points and their types, sets up the coefficient matrix $\boldsymbol{A}$ and calculates its inverse, $\boldsymbol{A}^{-1}$, of Eqs. (10) and (11). During each cycle of computation, the program updates the vector $\boldsymbol{b}^{(n)}$ and determines the ghost values of pressure. To test the effectiveness and accuracy of the boundary treatment, numerical simulation of acoustic wave scattering by circular cylinder and bodies with sharp edges were performed. The results are reported subsequently.

For the purpose of comparison with the present approach, we note that Ling,[22,23] Ling and Smith,[24] and Khan et al.[25] recently have published numerical results of acoustic wave scattering by cylinders and other objects. However, a closer look reveals that these authors did not actually perform wave scattering computations. They recast the problem into a radiation problem. The sound was generated by the nonhomogeneous boundary condition on the surface of the body. Ling[22,23] carried out a frequency-domain computation using a low-order finite difference scheme (the spatial resolution was not explicitly given in the paper). Khan et al.[25] implemented a finite volume code and time marched the solution to a steady periodic state using a spatial resolution of approximately 20 mesh spacings per wavelength. Such a fine resolution is required by the low-order finite volume scheme. Because of this, they were forced to limit

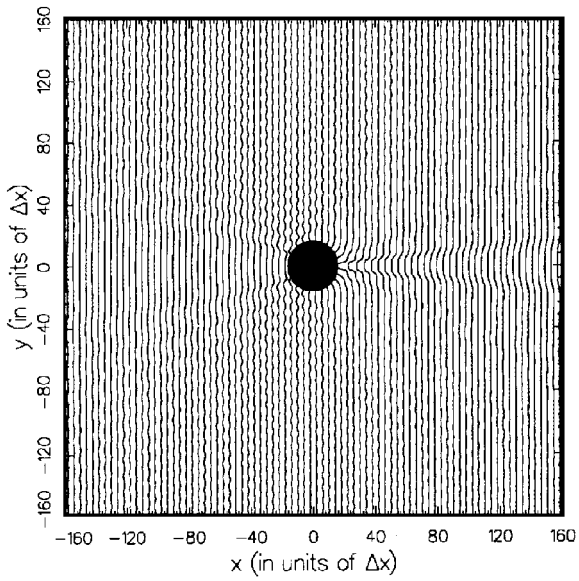

Fig. 9a Map of zero pressure contours at the beginning of a cycle associated with the scattering of plane acoustic waves by a solid cylinder; $D/\lambda = 4, \lambda = 8\Delta x$: ——, numerical and . . . . , exact.

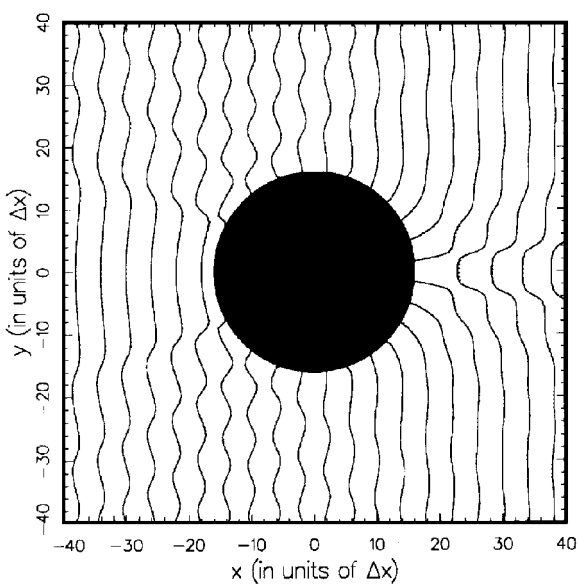

Fig. 9b Enlarged figure around the solid cylinder; $D/\lambda = 4, \lambda = 8\Delta x$: ——, numerical and . . . . , exact.

the size of their computation domain to a distance of no more than $1\frac{1}{2}$ wavelengths from the body. As a result, their results were not representative of far-field scattered wave solutions.

The numerical results of four test cases will now be presented. We will use $\Delta x (\Delta y = \Delta x)$, the mesh spacing, as the length scale. The spatial resolution is taken to be 8 mesh spacings per acoustic wavelength. This is close to the minimum resolution of 7–8 mesh spacings per wavelength required of the 7-point stencil DRP scheme as discussed in Ref. 3. We believe that any increase in spatial resolution will undoubtedly improve the quality of the computed results. The time step used in the z is $\Delta t = 0.05$. The DRP scheme is a four-level time marching scheme. Thus, the effective Courant–Friedrichs–Lewy number is 0.2. Artificial selective damping is imposed as described in Sec. IV. The results reported here are those that have been time marched to a periodic state with a maximum relative error over a period of 10^{-5}.

A. Scattering of Plane Acoustic Waves by a Circular Cylinder

The case of scattering of plane acoustic waves by a circular cylinder was investigated. The plane waves had a wavelength $\lambda = 8\Delta x$ and a wave vector pointing in the x direction. The cylinder diameter D was equal to 4λ. In the numerical simulation, a 320×320 grid was used with the cylinder placed right at the center. Nonhomogeneous radiation boundary conditions[26] were imposed at the boundaries of the computation domain. These boundary conditions generate the incoming acoustic waves and at the same time allow the scattered waves to leave the computational domain with little reflection. A zero initial condition was used to start the solution. After the transient disturbances exited the computation domain, the numerical solution settled down to a time-periodic state.

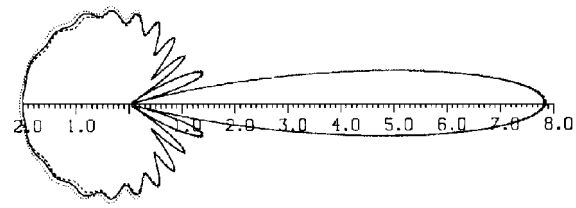

Fig. 10 Polar plot of the scattering cross section $\sigma(\theta)$ of a circular cylinder with $D/\lambda = 4$: ——, numerical, $\lambda = 12\Delta x$; ----, numerical, $\lambda = 8\Delta x$; and . . . . , exact at $r = 154\Delta x$.

Figure 9a shows the map of the computed zero pressure contours at the beginning of a period. In this figure, the shadow zone behind the cylinder can easily be seen. There are scattered waves radiating backward as well as to the upper and lower boundaries of the computation domain. Figure 9b shows an enlarged plot around the solid cylinder. This scattering problem has an exact solution.[27] The zero pressure contours of the exact solution are plotted as dotted lines in these figures. It is easily seen that there is good agreement between the numerical results and the exact solution.

The pressure associated with the scattered waves, p_s, is equal to the difference between the computed solution and the incident wave. The scattering cross section $\sigma(\theta)$ is defined by

$$\sigma(\theta) = \lim_{r \to \infty} (r \overline{p_s^2})^{\frac{1}{2}}$$

where an overbar denotes time average. Figure 10 shows the computed and the exact scattering cross section. There is good agreement between the computed and the exact solution, especially when improved numerical resolution ($\lambda = 12\Delta x$) is used. The improved numerical resolution provides a better approximation of the boundary curve.

B. Scattering of Plane Acoustic Waves by a Thin Plate

To test the ability of the proposed Cartesian boundary treatment to handle wave scattering by sharp edges, the problem of scattering of plane acoustic waves by a thin plate (as shown in Fig. 11) was investigated. A computation domain of 100×100 was used. The incident waves approached the thin plate at a 45-deg angle. The plate had a thickness of $0.2\Delta x$ and tapered off to zero thickness at the two ends. The length of the plate was $1\frac{1}{2}$ wavelengths. The plate was simulated by a row of type 3.3 ghost points.

The computed pressure field of the scattered waves along the upper boundary of the computation domain ($y = 45\Delta x$) at the beginning and at a quarter of a period later are given in Fig. 12. There is no exact solution to the thin plate problem. However, a good approximation of a thin plate is a plate with zero thickness. The zero thickness plate problem has an exact solution in terms of Mathieu functions. Here, for comparison purposes, the zero thickness plate solution computed in the same way as in Ref. 5 is used. This solution is shown as dotted lines in Fig. 12. There is good agreement between the two solutions, indicating that the present ghost point boundary treatment is effective and accurate, even for objects with sharp edges.

C. Scattering by a Lens-Shaped Airfoil

To provide further testing of the proposed boundary treatment for bodies with curved smooth surfaces as well as sharp edges, the case of a lens-shaped airfoil was considered. In the numerical computation, the incident acoustic waves were generated by a source in the energy equation [the fourth component of Eq. (1)]. The source

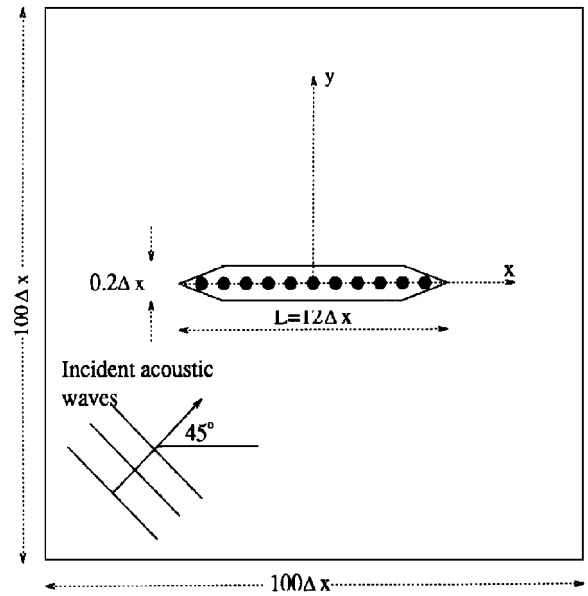

Fig. 11 Computational domain showing plane acoustic waves incident at an angle of 45 deg on a thin plate with sharp edges.

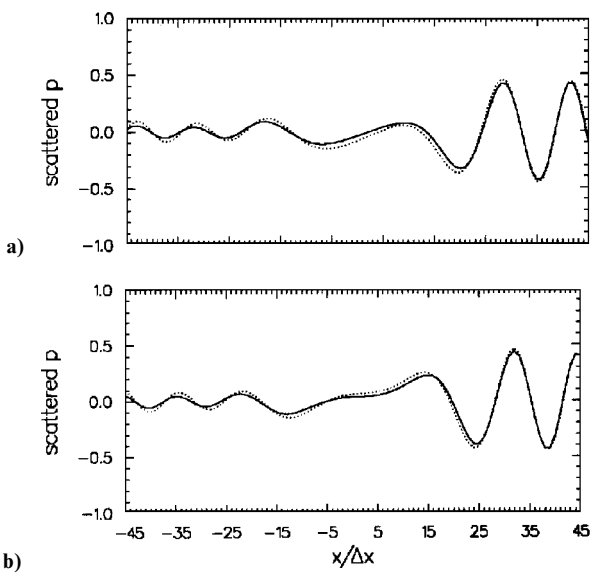

Fig. 12 Comparisons between the computed —— and the exact (zero thickness plate) . . . . . pressure distribution of the scattering waves along the line $y = 45\Delta x$; $\lambda = 8\Delta x$: a) at the beginning of a cycle and b) at a quarter of a cycle later.

had a spatial distribution in the form of a Gaussian function with a half-width of $3\Delta x$ centered at $x = -32\Delta x$, $y = 0$ in a 100×100 computation domain; i.e.,

$$Q(x, y, t) = 0.01\exp\{-\ln 2[(x + 32)^2 + y^2]/9\}\sin \omega t$$

The airfoil was formed by two large circular arcs with a maximum thickness of $2\Delta x$ and a chord length of $18\Delta x$. The airfoil, inclined at 45 deg to the x axis, was placed at the center of the computation domain. Because the noise source was inside the computation domain, radiation boundary conditions[4] were used in the numerical simulation.

Figure 13 is the map of the zero sound pressure contours of the computed acoustic field at the beginning of an oscillation cycle. In addition to the shadow zone to the right of the airfoil, there are strong reflected waves just above the airfoil. Such reflected waves are anticipated because the left surface of the airfoil is exposed to the incident waves at a 45-deg angle. There is no exact solution to the problem. To provide a measure of accuracy, the numerical computation was repeated using twice the spatial resolution. The

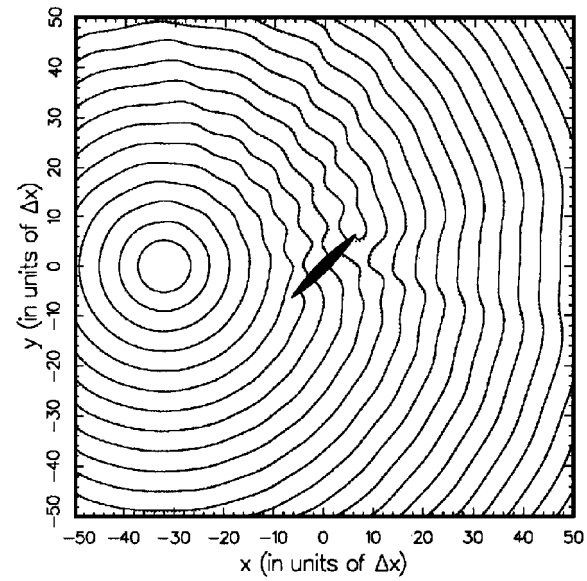

Fig. 13 Map of zero pressure contours at the beginning of a cycle associated with the scattering of acoustic waves by a lens-shaped airfoil; $\lambda = 8\Delta x$: ——, numerical solution and . . . . , numerical solution with twice the spatial resolution.

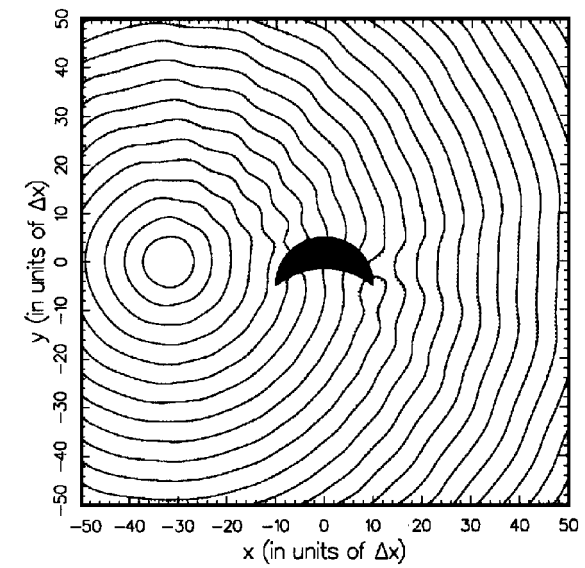

Fig. 14 Map of zero pressure contours at the beginning of a cycle associated with the scattering of acoustic waves by a double-concave-shaped airfoil: $\lambda = 8\Delta x$: ——, numerical solution and . . . . , numerical solution with twice the spatial resolution.

results of this computation are plotted as dotted lines in Fig. 13. For all intents and purposes, there is little difference between the two numerical solutions. We take this to be an indication that further mesh refinement is unnecessary because the computed solution is already fairly accurate.

D. Scattering by an Airfoil with a Concave Surface

In the preceding example, the bodies are convex in shape. To test the accuracy and effectiveness of the proposed boundary treatment when applied to a concave surface, the problem of scattering by an airfoil with a concave surface (as shown in Fig. 14) was studied. The airfoil was formed by a semicircle of radius $10\Delta x$ intersecting a circular arc of radius $(244)^{1/2}\Delta x$. In this test problem, the acoustic field was generated by the same noise source as the previous problem.

Figure 14 shows the map of the computed zero pressure contours at the beginning of an oscillation cycle. There are obvious differences between the sound field on the concave surface on the

bottom and that around the convex surface on top. Exact solution of the present problem is again unavailable. Shown in dotted lines in Fig. 14 is the numerical solution with twice the spatial resolution. The agreement between the two solutions is good.

VI. Conclusion

A Cartesian boundary treatment of solid surfaces had been developed specifically for use in conjunction with high-order finite difference schemes. The heart of the scheme lies in simulating these surfaces by ghost values of pressure. The ghost values are determined so that the wall boundary conditions are satisfied at the boundary surface. Numerical examples are provided to demonstrate the effectiveness and accuracy of the proposed method.

As pointed out at the beginning, in CFD Cartesian boundary treatment is not as popular as the use of body-fitted grids or unstructured grids. However, the same cannot be said for CAA. Thus far, CFD has not been proven to be an accurate and efficient method for solving CAA problems.[3] Thus, the present Cartesian boundary treatment, despite its complexities, clearly offers a viable option should accurate numerical solutions be required.

The basic ideas of the present ghost point method are easy to understand. But on implementation, a fair amount of programming complexities exists. This may require nontrivial initial development costs. Yet such costs are incurred primarily once. For this reason, they should not be a deterrent to its use in solving aeroacoustics problems.

The present method approximates the body by straight line segments. The accuracy of this approximation improves greatly with mesh refinement. It is also well known that the efficiency of Cartesian boundary treatment also improves with mesh refinement, as the number of computation operations in the computation domain increases much faster than that along the wall boundaries. This is a significant advantage and should not be overlooked.

Acknowledgment

This work was supported in part by NASA Langley Research Center Grant NAG 1-1479.

References

[1]Steger, J. L., and Benek, J. A., "On the Use of Composite Grid Schemes in Computational Aerodynamics," *Computer Methods in Applied Mechanical Engineering*, Vol. 64, 1987, pp. 301–320.

[2]Venkatakrishnan, V., "A Perspective on Unstructured Grid Flow Solvers," Inst. for Computer Applications in Science and Engineering, ICASE Rept. 95-3, Feb. 1995.

[3]Tam, C. K. W., "Computational Aeroacoustics: Issues and Methods," *AIAA Journal*, Vol. 33, No. 10, 1995, pp. 1788–1796.

[4]Tam, C. K. W., and Webb, J. C., "Dispersion-Relation-Preserving Finite Difference Schemes for Computational Acoustics," *Journal of Computational Physics*, Vol. 107, Aug. 1993, pp. 262–281.

[5]Tam, C. K. W., and Dong, Z., "Wall Boundary Conditions for High-Order Finite Difference Schemes in Computational Aeroacoustics," *Theoretical and Computational Fluid Dynamics*, Vol. 6, No. 6, 1994, pp. 303–322.

[6]Gaffney, R. L., Hassan, H. A., and Salas, M. D., "Euler Calculations for Wings Using Cartesian Grids," AIAA Paper 87-0356, 1987.

[7]Clarke, D. K., Salas, M. D., and Hassan, H. A., "Euler Calculations for Multielement Airfoils Using Cartesian Grids," *AIAA Journal*, Vol. 24, No. 3, 1986, pp. 353–358.

[8]Berger, M. J., and Le Veque, R. J., "An Adaptive Cartesian Mesh Algorithm for the Euler Equations in Arbitrary Geometries," AIAA Paper 89-1930, 1989.

[9]Berger M. J., and Colella, P., "Local Adaptive Mesh Refinement for Shock Hydrodynamics," *Journal Computational Physics*, Vol. 82, 1989, pp. 64–84.

[10]Young, D. P., Melvin, R. G., Bieterman, M. B., Johnson, F. T., Samant, S. S., and Bussoletti, J. E., "A Locally Refined Rectangular Grid Finite-Element Method: Application to Computational Fluid Dynamics and Computational Physics," *Journal of Computational Physics*, Vol. 92, 1991, pp. 1–66.

[11]Chiang, Y-L, van Leer, B., and Powell, K. G., "Simulation of Unsteady Inviscid Flow on an Adaptively Refined Cartesian Grid," AIAA Paper 92-0442, 1992.

[12]Bayyuk, S. A., Powell, K. G., and van Leer, B., "A Simulation Technique for 3-D Unsteady Inviscid Flows Around Arbitrarily Moving and Deforming Bodies of Arbitrary Geometry," AIAA Paper 93-3391, 1993.

[13]Coirier, W. J., and Powell, K. G., "An Accuracy Assessment of Cartesian Mesh Approaches for the Euler Equations," AIAA Paper 93-3335, 1993.

[14]Falle, S. A. E. G., and Giddings, J., "Body Capturing Using Adaptive Cartesian Grids," *Numerical Methods in Fluid Dynamics*, Vol. 4, 1993, pp. 337–343.

[15]Melton, J. E., Enomoto, F. Y., and Berger M. J., "3D Automatic Cartesian Grid Generation for Euler Flows," AIAA Paper 93–3386, 1993.

[16]Pember, R. B., Bell, J. B., Colella, P., Crutchfield, W. Y., and Welcome, M. L., "Adaptive Cartesian Grid Methods for Representing Geometry in Inviscid Compressible Flow," AIAA Paper 93-3385, 1993.

[17]De Zeeuw, D., and Powell, K. G., "An Adaptively Refined Cartesian Mesh Solver for the Euler Equations," *Journal of Computational Physics*, Vol. 104, 1993, pp. 56–68.

[18]Quirk, J. J., "An Alternative to Unstructured Grids for Computing Gas Dynamic Flows Around Arbitrarily Complex Two-Dimensional Bodies," *Computers and Fluids*, Vol. 23, 1994, pp. 125–142.

[19]Quirk, J. J., "A Cartesian Grid Approach with Hierarchical Refinement for Compressible Flows," Inst. for Computer Applications in Science and Engineering, ICASE Rept. 94-51, June 1994.

[20]Chung, C., and Morris, P. J., "A New Boundary Treatment for Two- and Three-Dimensional Acoustic Scattering Problems," First Joint Confederation of European Aerospace Societies/AIAA Aeroacoustics Conf., CEAS/AIAA Paper 95-008, Munich, Germany, June 1995.

[21]Tam, C. K. W., Webb, J. C., and Dong, Z., "A Study of the Short Wave Components in Computational Acoustics," *Journal of Computational Acoustics*, Vol. 1, March 1993, pp. 1–30.

[22]Ling, R. T., "Numerical Solution for the Scattering of Sound Waves by a Circular Cylinder," *AIAA Journal*, Vol. 25, No. 4, 1987, pp. 560–566.

[23]Ling, R. T., "Finite-Difference Approach to Scattering of Sound Waves in Fluids," *AIAA Journal*, Vol. 26, No. 2, 1988, pp. 151–155.

[24]Ling, R. T., and Smith, T. D., "Scattering of Acoustic and Electromagnetic Waves by an Airfoil," *AIAA Journal*, Vol. 27, No. 3, 1989, pp. 268–273.

[25]Khan, M. M. S., Brown, W. H., and Ahuja, K. K., "Computational Aeroacoustics as Applied to the Diffraction of Sound by Cylindrical Bodies," *AIAA Journal*, Vol. 25, No. 7, 1987, pp. 949–956.

[26]Tam, C. K. W., Fang, J., and Kurbatskii, K. A., "Nonhomogeneous Radiation and Outflow Boundary Conditions Simulating Incoming Acoustic and Vorticity Waves for Exterior Computational Aeroacoustics Problems," *International Journal of Numerical Methods in Fluids* (submitted for publication), 1996.

[27]Morse, P. M., and Ingard, K. U., *Theoretical Acoustics*, McGraw–Hill, New York, 1968.